Charge transport properties of Ru-complex molecules: the influence of humidity

Atesci, H.

4. Switchable diode behavior in 2-Ru-N molecular layers

In this chapter, we will present experimental current-voltage data on the **1-Ru-N**, **1-Ru-Py**, and **2-Ru-N** SAMs in both dry (≈5% relative humidity) and humid (≈60% relative humidity) conditions. We will find that upon changing the atmospheric humidity, **2-Ru-N** shows a very remarkable result. Namely, its current-voltage characteristic switches from anti-symmetric (in dry conditions) to very asymmetric diode-like (in humid conditions).

We will provide a discussion of this intriguing result in the light of an elastic tunneling model and DFT calculations with which we can build the framework of our model. We will touch upon a tentative Gorsky model to discuss the relationship between the current-voltage characteristic and the exerted force and tip radius. Also, we will discuss possible contributions from inelastic hopping transport.

This work is published as: Huseyin Atesci, Veerabhadrarao Kaliginedi, Jose A. Celis Gil, Hiroaki Ozawa, Joseph M. Thijssen, Peter Broekmann, Masa-aki Haga, Sense Jan van der Molen, Humidity-controlled rectification switching in ruthenium-complex molecular junctions. *Nature nanotechnology* **13**, 117 (2018).

4.1 Introduction

As discussed in Chapter 1, molecular rectifiers were first proposed over four decades ago(*1, 75-77*). However, the realization of the molecular rectifier was an exceptionally difficult task, as exemplified by the rather moderate(*34, 77-84*) values of the reported rectification ratio (RR) of ~15. Recently, this ceiling was convincingly broken by the groups of Nijhuis(*63*), Venkataraman(*62*), and Diez-Pérez(*85*).

Nijhuis used an E-GaIn top contact to probe molecular monolayers of coupled ferrocene groups and obtained progressively higher rectification ratios, recently reaching 10^5. Venkataraman employed STM-break junctions to probe single molecules and reported RR≈200. The latter rectification effect was explained from the geometric asymmetry in the double layers formed around tip and substrate(*62, 86*). Also, high rectification (RR>100) was also observed in mechanical break junction experiments(*87, 88*).

In this chapter, we will explore the effects of humidity on the I-V characteristics, and more specifically, the rectification of Ru-complexes (the specific molecules being **1-Ru-N**, **1-Ru-Py** and **2-Ru-N**, see also Chapter 1.5). We will show over the course this chapter that out of this selection of molecules, **2-Ru-N** has remarkable properties in that it exhibits both humidity sensitive rectification and very high RR-values, reaching ~10^4. After showing the necessary control measurements, we will move on to providing a tentative model to explain these results.

4.2 Experiment

Experimentally, we employ conductive-probe atomic force microscopy (C-AFM)(*32, 89*) to measure I-V-characteristics of self-assembled monolayers (SAMs) of three types of Ru-complexes on indium-tin-oxide (ITO), see Figure 4.1. The mono-nuclear **1-Ru-N** and di-nuclear **2-Ru-N** molecules contain tetrapodal phosphonic acid anchoring groups, symmetrically on both sides. The mono-nuclear **1-Ru-Py** molecule, however, is asymmetric, with a tetrapodal phosphonic acid anchoring group at one side and a pyridine group at the other.

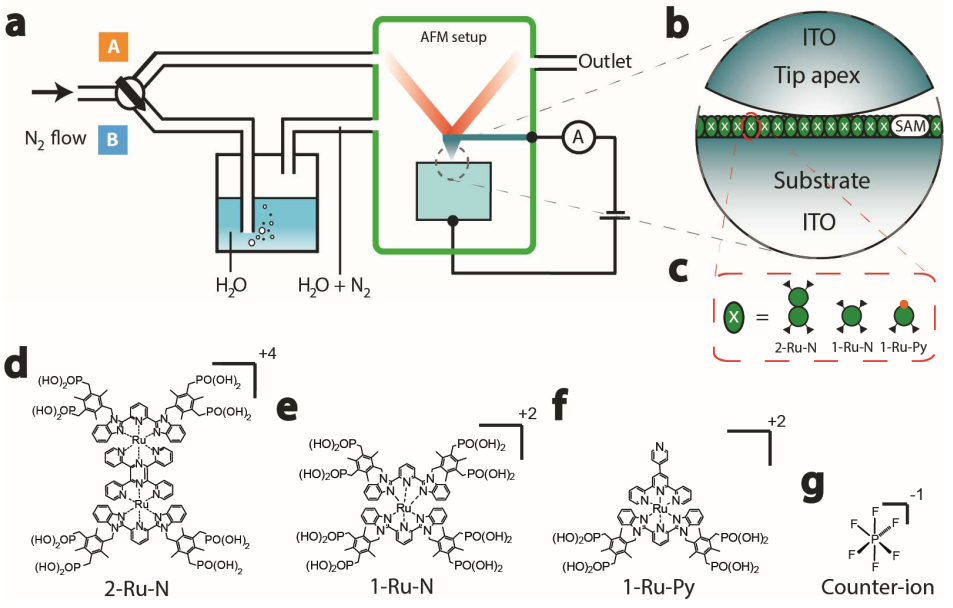

Figure 4.1: Schematic representation of the experimental setup and molecular systems studied. (a) The system can be purged with either dry N_2 (A) or humid N_2 (B), when N_2 is bubbled through Milli-Q water. The latter case is shown. (b) A schematic representation of the ITO-molecule-ITO junction. Three different types of molecules are used (c). Their (charged) molecular structures are shown in (d-f). In all cases PF_6^-(g) acts as the counter-ion in the SAM.

We have also provided electrochemical characterization of these molecules in Chapter 3.2.1, where the cyclic voltammograms of **2-Ru-N** show two redox peaks (in 0.1M $HClO_4$ in CH_3CN). These correspond to the oxidation of Ru(II)–Ru(II) $\Longrightarrow$ Ru(III)–Ru(II) and Ru(III)–Ru(II) $\Longrightarrow$ Ru(III)–Ru(III), respectively, signifying the strong electrostatic coupling of the two Ru-centers. The mono-nuclear Ru-complexes **1-Ru-Py** and **1-Ru-N** show one redox peak only, corresponding to the oxidation of both Ru-centers simultaneously Ru(II) $\Longrightarrow$ Ru(III).

For the conductance experiments, we coat the AFM probes with ITO by sputter coating. This is done to make sure that the top contact (AFM-tip) and bottom contact (ITO substrate) are chemically symmetric (In Chapter 5, we will explore the effects of chemical asymmetry, using Au-coated top electrodes).

Next, current-voltage (I-V) characteristics are determined by contacting the SAMs with a C-AFM-probe at a force setpoint of typically 10.5 nN (See Section 3.4.1). As the number of molecules trapped between the two ITO-electrodes may vary (roughly ~100), we take hundreds of I-V curves at different spots on the sample(*32*). All experiments are done at room temperature in an atmosphere where we can control the humidity by purging either with dry N_2 (resulting in ≈5% humidity) or humid N_2 resulting in ≈60% humidity), see also Fig. 4.1.

4.3 Results

In Figure 4.2b, and 4.2c, we present transport measurements on **2-Ru-N** junctions at low and high relative humidity, respectively. Results are shown in the form of 2D histograms of the logarithm of the absolute current vs. voltage. This is done for two reasons. First, it allows us to display all measurements in a single plot (only if a short is observed, do we omit the data). Second, it reveals the presence (or absence) of symmetry in I-V-characteristics. Also shown in these figures are logarithmic averages of the current (lines), including error bars determined from the half width of the Gaussian fits to the logarithm of the current values at each voltage considered.

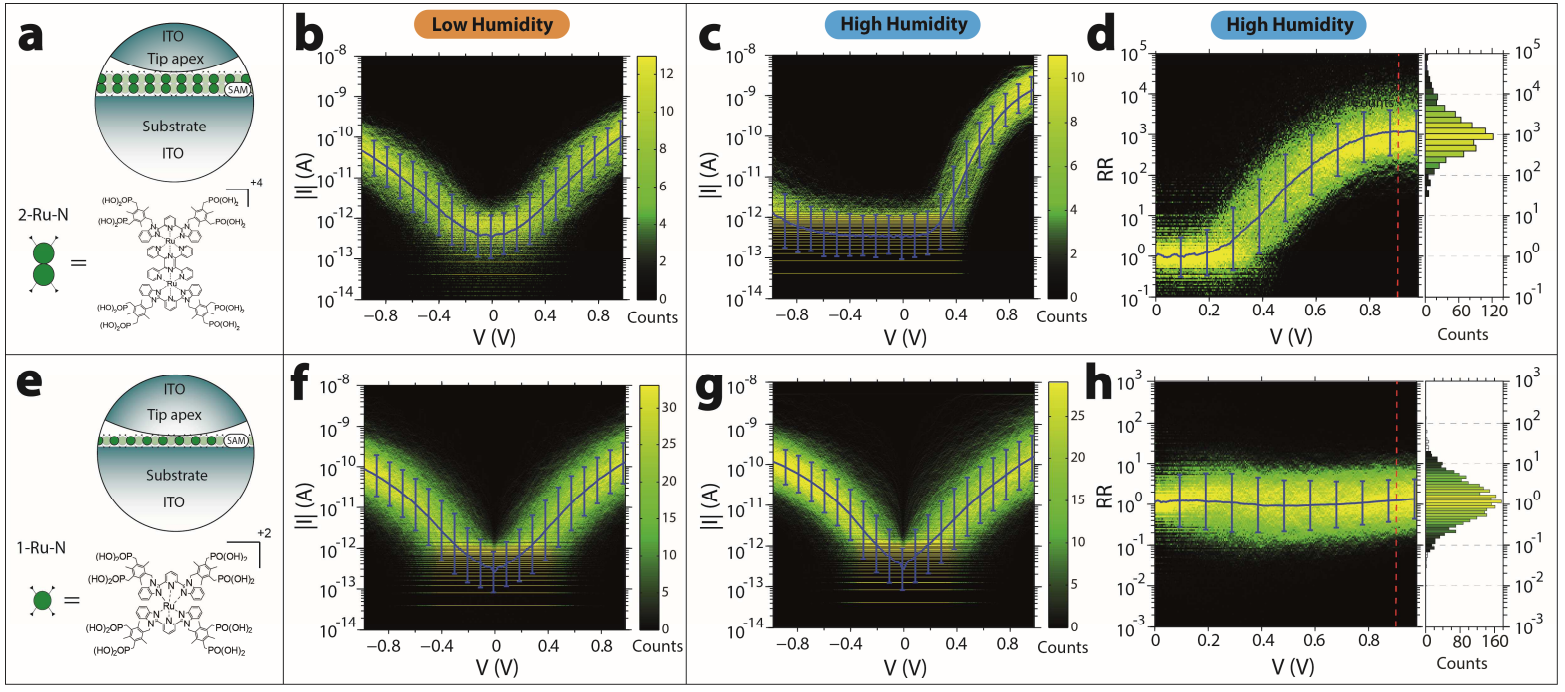

Figure 4.2: (a), (e): Schematic representation of the **2-Ru-N** (a) and **1-Ru-N** (e) ITO-molecule-ITO junctions. (b), (c): 2D-histograms of logarithmically binned |I|-V characteristics of **2-Ru-N** molecular junctions for: (b) low humidity (5%) and (c) high humidity (60%) conditions. (d): 2D-histogram of logarithmically binned RR-V for the humid case; *right:* 1D-histogram taken at V=0.9 V. (f), (g): 2D-histogram of |I|-V curves of **1-Ru-N** for: (f) low humidity (5%) and (g) high humidity (60%) conditions. (h): 2D-histogram of logarithmically binned RR-V for the humid case; *right:* 1D-histogram taken at V=0.9 V. Overlaid in blue in (b-d, and f-h) is the mean of the Gaussian fits at each bias voltage bin. The error bars follow from the half widths of the fits. For all measurements shown here, a tip radius of 150 nm was used.

As seen in Figure 4.2, humidity has a remarkable effect on the I-V-characteristics of **2-Ru-N** junctions. The |I|-V-characteristics recorded in 'dry' conditions are nearly symmetric (Fig. 4.2b), whilst the high-humidity curves are diode-like (Fig. 4.2c). To quantify this further, we calculate the rectification ratio (RR) at each voltage, defining RR(V)=|I(+V)/I(-V)|. For the 'dry' case, we find RR-values close to unity over the entire V-range. For humid conditions, however, we observe RR~1000 for V>0.7 V (Fig. 4.2d). We have fitted the log(RR)-data to Gaussians at each V (see Chapter 3.6): In dry conditions, we find $RR_{dry}=10^{0.4\pm0.4}$ at 0.9 V, dramatically lower than for high humidity, for which $RR_{humid}=10^{3.0\pm0.6}$ at 0.9 V.

To benchmark these results, we also studied **1-Ru-N** SAMs (see Fig. 4.2e-h). Interestingly, their |I|-V characteristics are nearly symmetric, independent of humidity. Also, the chemically asymmetric **1-Ru-Py** SAMs show nearly symmetric transport, in dry and humid conditions, (see Fig. 4.3).

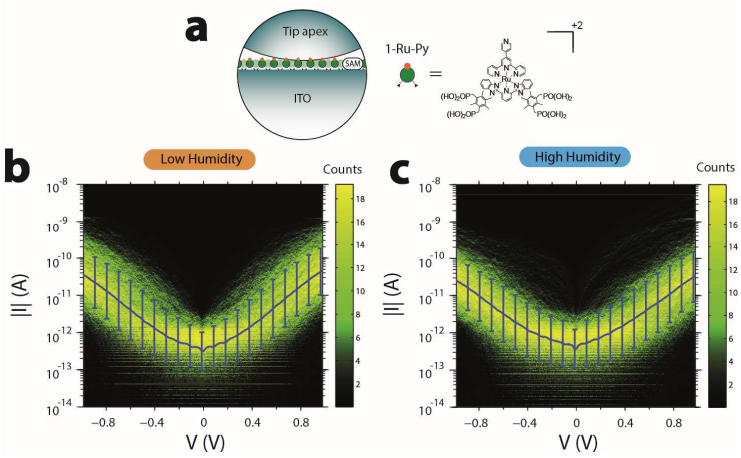

Figure 4.3: Schematic representation of the **1-Ru-Py** molecular junction during measurement (a). 2D-histograms of logarithmically binned |I|-V characteristics of **1-Ru-Py** molecular junctions for: (b) low humidity (5%) and (c) high humidity (60%) conditions. Overlaid in blue in (b,c) is the mean of the Gaussian fits at each bias voltage bin. The errorbars follow from the half widths of the fits.

Figure 4.4a compares the rectification ratios, as measured for the three molecules considered, in one view. Specifically, it displays RR(V=0.9 V), for repeated toggling between dry and humid conditions. The most dramatic effect is clearly seen for **2-Ru-N**: its RR changes from ~1 (dry) to ~1000 (humid) for three cycles without degradation. The other two molecules, **1-Ru-N** and **1-Ru-Py**, show negligible rectification in all cases.

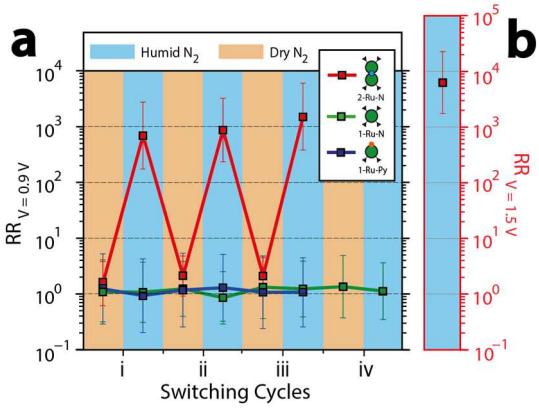

Figure 4.4: (a): RR(V=0.9 V) for consecutive measurements on **2-Ru-N** (red line), **1-Ru-N** (green line) and **1-Ru-Py** (blue line), in humid and dry conditions (tip radius: 150 nm). Changing between low (≈5%) and high (≈60%) humidity takes

approximately 30 minutes, and measurements for each value of the humidity last 1-2 hours. (b): measurement with reduced noise floor and sharper tip (50 nm radius), yielding an improved lower bound for RR in high humidity conditions (see Fig. 4.6), is shown separately.

While Figs. 4.2, 4.3 and 4.4a were obtained using a 150-nm tip, we additionally used tips with radii 50 and 500 nm. To keep the pressure approximately the same, we adapt the force applied, following the work of Carpick *et al.*(*71*) (see Fig. 4.5a) and Section 3.4.1). In Fig. 4.5b, we show the results, for **2-Ru-N** in humid conditions. Interestingly, we find that smaller tip radii result in higher RR-values.

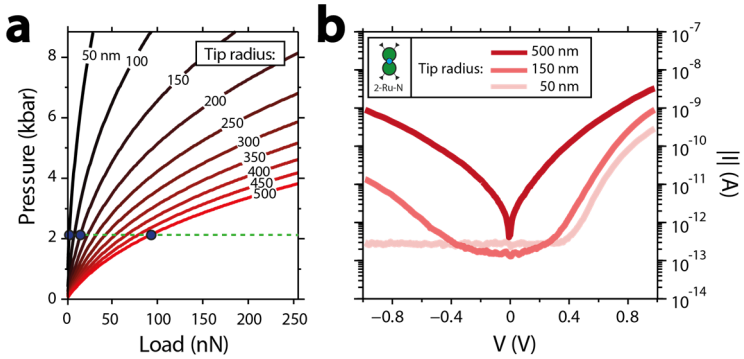

Figure 4.5: (a) Theoretical curves of the pressure on the SAM versus tip load with varying tip radii. The parameters and formulae used for this approximation is derived from the paper from Carpick et al(*71*). From the force values extracted from (a), we performed tip radius dependent measurements while keeping the calculated pressure values approximately constant for all tip radii (b). Different tip radii (50, 150, and 500 nm) were used to contact the **2-Ru-N** SAMs at high humidity. We used force setpoints of 2.8, 10.5, 70 nN, respectively, to achieve approximately the same pressure for all three cases. Note that in (b), the means of the Gaussian fits to the absolute current |I| are plotted vs. voltage V; the full |I|-V histograms can be seen in the Appendix Figure A.4.

This particular data set was made with a lower time for self-assembly (3 times less deposition time). We note that the data set made with a 150 nm tip has a lower RR compared to those seen in Figs. 4.2c,d. Thus, deposition time is also an important factor that will determine the scale of the RR value. We did not however, research the effect of deposition time on the RR in detail and thus it will remain outside the scope of this thesis.

In Fig. 4.5b, we can also note that the RR values for the 50 nm tip in Fig. 4.5b are still limited by the current noise floor. We can reduce the noise floor by significantly reducing the voltage sweep rate to 0.02 Hz and changing the current sensitivity to 20 pA/V with low bandwidth. With these changes, it is possible to further reveal the current data at negative voltages, as shown in Fig, 4.6, where we find RR-values as high as $10^{3.8\pm0.6}$ ≈6500 (plotted in Fig. 4.4b). Still, even this value, unprecedented in literature within a bias range of ±1.5V, represents a lower limit, since most current values at negative voltage values are still below the (improved) noise level.

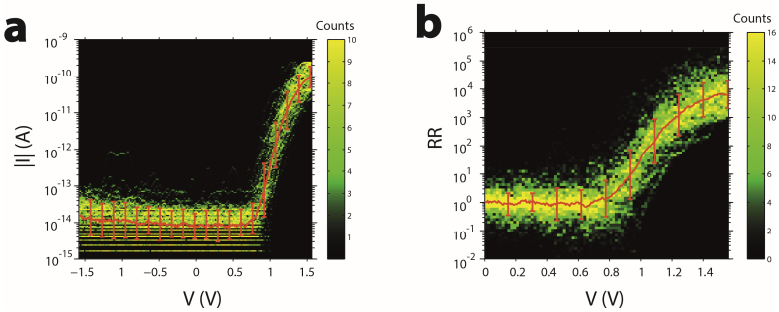

Figure 4.6: (a) 2D-histogram of logarithmically binned |I|-V characteristics of junctions of **2-Ru-N** during high humidity conditions measured with a 50-nm tip. (b) The corresponding 2D-histogram of logarithmically binned RR values against the bias voltage V. Overlaid in red is the mean of the Gaussian fits at each bias voltage bin. The error bars follow from the half widths of the fits.

Next, we varied the applied force, for certain tip radii. As the force is reduced, RR-values increase, see Figure 4.7b. We have also included Au-coated tips, which produce very similar I-V characteristics. We will defer the discussion of the addition of Au as an extra material to the following chapter. What is important to note, however, is that for both Au and ITO-coated tips, higher forces result in less rectification for the **2-Ru-N** junction, see Figure 4.7b. When the tip is withdrawn slightly whilst being in the snap-off regime, we will effectively reduce its contact area with the junction. This we define as 'negative force' in Figure 4.7b. The 'ITO 50 nm' seemingly produce a trend contradicting the rest of the data. This is however, an artifact, due to the noise floor limiting the RR, see Figure 4.7a.

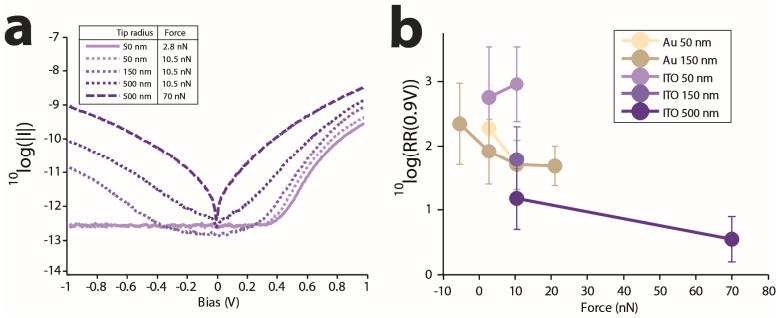

Figure 4.7: Logarithmically plotted averaged |I|-V data for different ITO-coated tip radii and forces (a). Logarithmically plotted RR values at 0.9 V against the exerted force for different tip radii and forces (b).

For completeness, we also studied the I-V-characteristics of bare ITO-ITO junctions for low and high humidity, finding symmetric |I|-V curves with high conductance, see Fig. A.5 of the Appendix.

4.4 Discussion

Having experimentally established their extraordinary humidity-dependence, we proceed towards a transport model of these **2-Ru-N** junctions. Given the complexity of the system, containing large molecules, two geometrically different (though chemically similar) ITO-electrodes, counter-ions, and water molecules at the junction interface(*90*), we aim at elucidating the essentials.

In a system where the current is modelled with a single molecular orbital, a well-established reason for rectification is an asymmetry in the voltage drop over the metal-molecule-metal junction, as we have explained in Chapter 2.3, rectification may occur due to several reasons. Relevant for us is the rectification caused by difference in the curvature of the electrodes in an electrolytic environment, theorized by Cheung *et al.(86).*

This had been observed experimentally by the group of Venkataraman (*62*), where rectification was observed in a similar junction geometry as in our case, i.e. an STM break junction in an electrolytic environment. They also used a single level system with a voltage drop asymmetry to model their results. Our next logical step is thus to consider and discuss a similar approach of a single level model. If this is insufficient as an explanation, we can proceed moving into more complex models.

For the case where we consider the current to be dominated by a single molecular orbital (i.e. using a single level model), rectification will occur provided there is a voltage drop asymmetry at the electrode interfaces. The chemical potential of the molecular energy level is then 'pinned' to (and lifted with) the chemical potential to one particular electrode, causing rectification (see also Chapter 2.3). However, this mechanism predicts rectification irrespective of whether the molecule contains one or two Ru atoms. This is inconsistent with our data: The mono-nuclear variety **1-Ru-N**, with the same end groups as **2-Ru-N**, shows RR-values near unity in all conditions. Even the **1-Ru-Py** does not show strong asymmetries in its I-V-curves (Fig. 4.3a). So, level pinning by itself is not enough to explain our data, suggesting that the two-site Ru-structure of **2-Ru-N** is key to the mechanism.

The same argument can be made for the model that was used by the group of Nijhuis *et al.*, where they reported high rectification ratios on ferrocene-based molecular layers in an EGaIn setup (with no electrolyte)(*63*). There, they consider the levels localized on the ferrocene group that asymmetrically couple to electrodes via alkane barriers. For such structures, rectification is predicted even in dry conditions. Such models may be applicable to molecules with one Ru group (**1-Ru-N**, **1-Ru-Py**), but for these we do not observe significant rectification.

Summarizing, our data imply that two elements are essential: a) the structure of two Ru centres in series; b) water, somehow breaking the symmetry between these centres. A proper model should therefore take these observations into account.

For this, we require detailed calculations of the orbital structures of our Ru-complexes, in particular the **1-Ru-N** and **2-Ru-N** molecules as they have the same anchoring groups.

We have collaborated with J.A.C. Gil and J.M. Thijssen from the Theoretical Physics group from Delft University to study the orbital structures of the **1-Ru-N** and **2-Ru-N** complexes in detail with density functional theory (DFT) in combination with the Non-equilibrium Green's Function (NEGF) formalism (see Chapter 3.7), the details of which will be elaborated further.

For both **1-Ru-N** and **2-Ru-N**, we have found from the DFT calculations that the conduction is HOMO-dominated. Also, additional calculations have been performed on the lower lying energy levels to see whether there is interaction between these and the HOMO level.

4.4.1 DFT calculations on 1-Ru-N in presence and absence of water

Let us first focus on **1-Ru-N**. Figure 4.8a shows the orbital structures of the HOMO and HOMO-1 mono-nuclear Ru complexes. Clearly these orbitals have very different distribution and they do not have the same symmetry properties. This suggests that they can be treated as single levels that contribute individually to the current (**1-Ru-N** is studied here, but our calculations for **1-Ru-Py** yield a similar conclusion).

To substantiate this analysis, we have performed transport calculations using the non-equilibrium Green's function (NEGF) method as implemented into ADF(*91, 92*). To this end, a geometrical relaxation is made on the molecules (and counter-ions) to find the optimal structure in its ground state. Then, the molecules are coupled to wide-band-limit electrodes, after which the current is calculated for 110 bias values (ranging from -1.1 to 1.1 V), for dry conditions (no water molecules). The result of the NEGF method can be seen in the |I|-V characteristic (orange curve) shown in Figure 4.9a, which is basically symmetric. Based on Fig. 4.9a, we plot the calculation of the RR against V in Fig. 4.9b (orange curve), where RR values around 1 are indeed found.

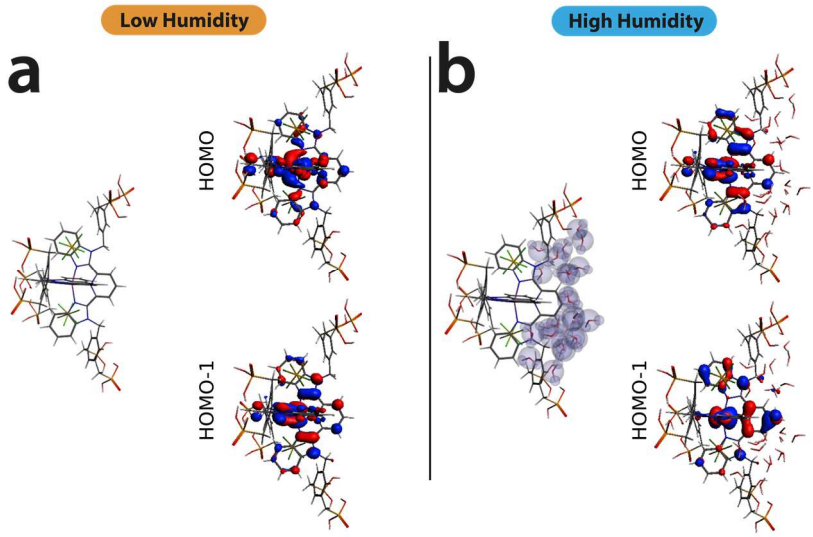

Figure 4.8: DFT-calculated wave functions of the HOMO and HOMO-1 for the **1-Ru-N** molecule (a) without and (b) with water molecules.

Next, we discuss the role of water. We anticipate that in humid conditions the tip attracts more water molecules than the surface, both due to the higher hydrophilicity of bare ITO compared to ITO modified with Ru-complexes and due to capillary effects(*90*). The water contact angle was measured both for precleaned bare ITO (37°) and for Ru-complex modified ITO (57°), demonstrating a significant difference in wettability. To find out how an enhanced water concentration at the tip-side affects electrostatics, explicit water molecules (in this case 28 molecules) have been added to the system. We assume water to primarily enter the SAM through the side which is exposed to air, which in the case of Fig. 4.8, is held at the right hand side of the molecule. Using multiple independent starting conformations where water is placed at the right hand side of the molecule, we consistently find after geometric relaxations that for **1-Ru-N**, the water molecules stay near the tip-side without crossing over to the other half (Fig 4.8b).

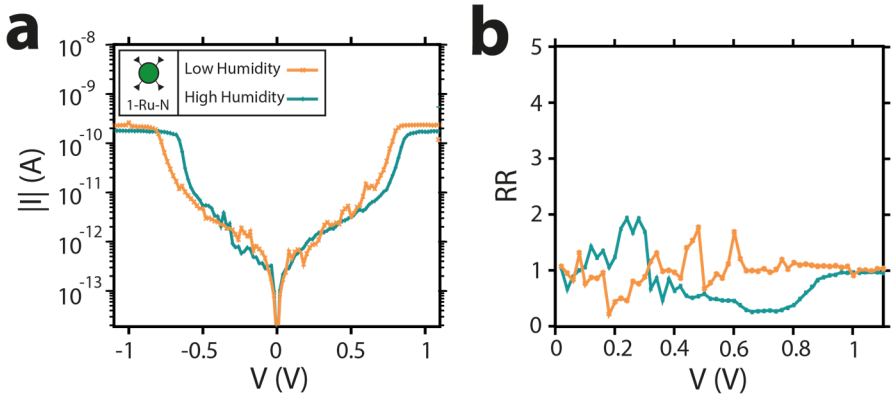

Figure 4.9: Current (a) and RR (b) calculated for **1-Ru-N** complex with and without water.

Also for **1-Ru-N** in humid circumstances (Fig. 4.8b), the orbital structures for the HOMO and HOMO-1 have a clearly different symmetry. Hence, both can be treated as single levels that contribute individually to charge transport. The calculated |I|-V characteristics also show that humidity has a small effect on current-voltage symmetry as can be seen in Figure 4.9 (blue curves). This small effect stems from the effect the electric field has on the water molecules, namely rotation and translation while incrementally changing the

bias. This results in a slight gating of the molecular orbital during bias sweep, resulting in a slightly different RR-V characteristic (blue curves). We will go into more detail into this aspect of our calculations in the following paragraph.

4.4.2 DFT calculations on 2-Ru-N in presence and absence of water

The **2-Ru-N** complex is quite different from **1-Ru-N**, both from an orbital and I-V characteristic perspective. Quantum chemistry calculations for gas-phase **2-Ru-N** (Fig. 4.10a) show that the highest occupied molecular orbital (HOMO) and the orbital slightly below it (HOMO-1), have an anti-symmetric and symmetric structure, respectively (Fig. 4.10b). Subtracting and adding these orbitals results in two 'localized molecular orbitals' (LMOs), which are nearly degenerate: one around the Ru near the tip, and one around the Ru near the substrate (Fig. 4.10c). If a bias is applied to such a molecule, these two levels shift apart, and the transmission decreases(*28*). Importantly, this happens symmetrically for positive and negative bias (see Figure 4.10c-e). This is basically our model for the 'dry case'.

As for the effect of water: at the tip side, the mere presence of water hydrates the counter-ions, pulling them out by ≈ 0.5 Å. This results in a change in the local electrostatic environment, shifting the chemical potential of the LMO near the tip down relative to the other LMO. Thus, the symmetry is broken at zero voltage bias already (Fig. 4.10h).

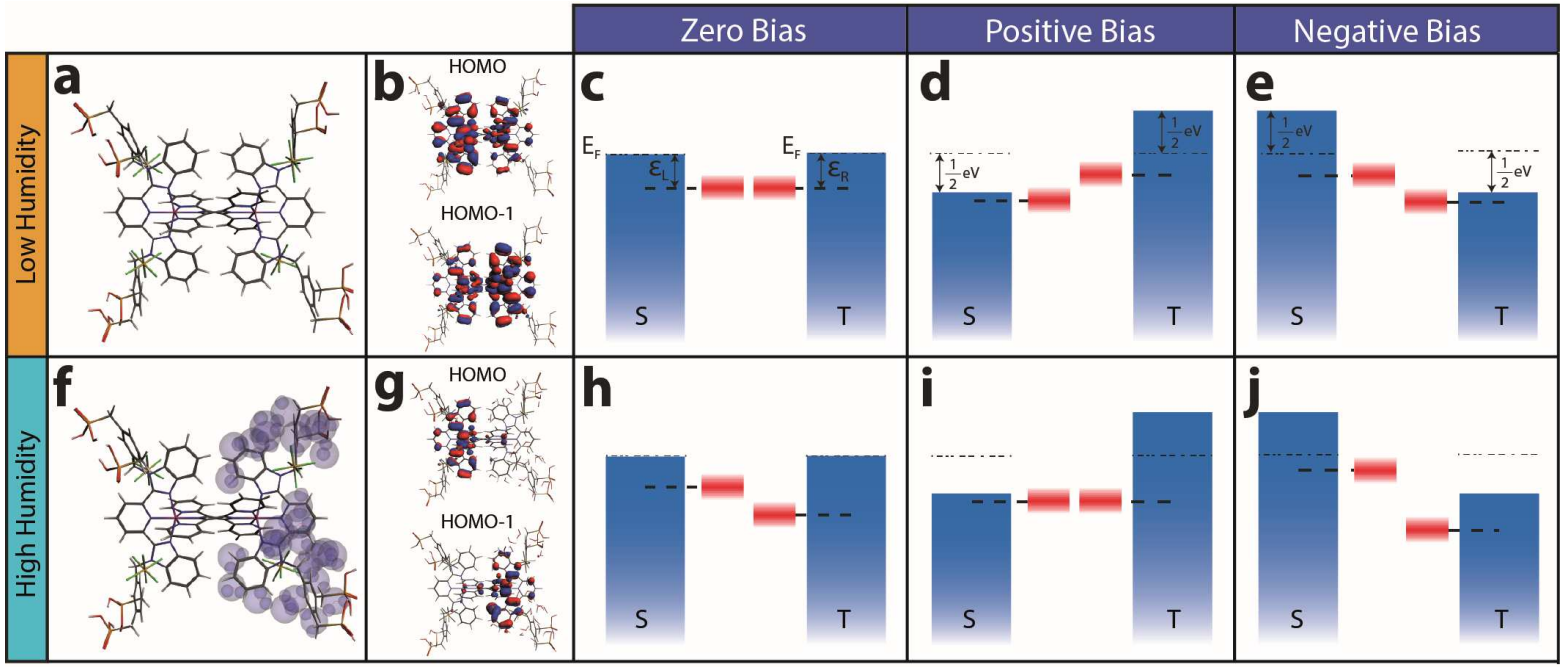

Figure 4.10: The **2-Ru-N** complex in simulated (a) dry conditions (f) humid conditions, with the purple dots representing water molecules. Without the presence of water, the HOMO and HOMO-1 orbitals show a symmetric and antisymmetric structure (b). In the presence of an asymmetric water distribution, the HOMO and HOMO-1 orbitals are more strongly localized on the substrate side and tip side Ru-centers respectively (g). Illustration of a two-site system between substrate and tip electrodes in dry conditions: the two LMOs are aligned at zero bias (c), which does not result in rectification as the current is equally suppressed for positive (d) and negative bias (e). In humid conditions: the LMO on the substrate side has a relatively higher chemical potential compared to the tip counterpart due to an asymmetric gating effect caused by the displacement of the counter-ions caused by the water molecules (h). This results in rectification, due to relatively high current when the levels come close to resonance (i) at positive bias, and strong current suppression when the levels misaligned at negative bias (j). In both dry and humid cases, the transport is assumed to be HOMO-HOMO-1 dominated. Note that our tip is grounded; a positive voltage refers to a positive voltage on the substrate.

For a more elaborate physical approximation, let us now incorporate a voltage bias. This is done within the model by applying a homogeneous electric field directed along the tip-surface axis (see Fig. 4.11). For each field intensity and for several initial conformations of the 28 water molecules incorporated, a geometric optimization was performed. An important parameter to note is that all calculations have been performed at an effective temperature of 0 K.

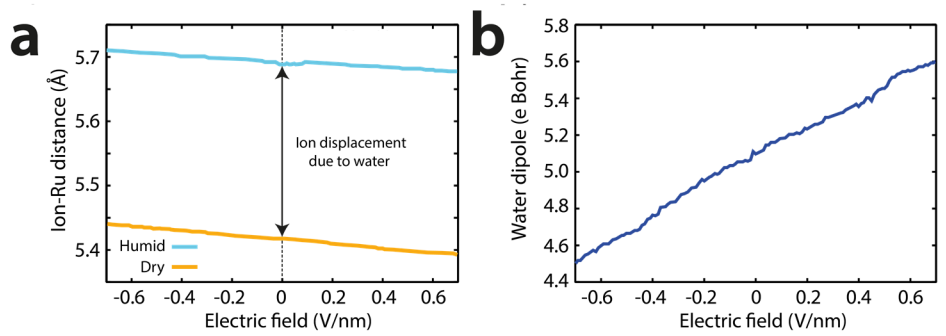

Figure 4.11: (a) Counter ion displacement as a function of the external electric field in dry and humid conditions. It can be seen that for humid conditions and zero external electric field, the ions are already displaced with respect to their positions at dry conditions. (b) Total dipole moment of the water molecules as a function of the external electric field (b). We can note that the water molecules are unlike bulk water, as they do not fully rotate during the bias sweep.

The calculations systematically show that for positive (substrate) bias, the counter-ions move away from the tip, closer to the molecule (Fig. 4.11a). For the case of **2-Ru-N**, this pushes the chemical potential of the LMO near the tip upwards, towards that of the other LMO. As the two levels align, transport is enhanced (Fig. 4.10i). For negative biases, however, the counter-ions move away from the molecule (Fig. 4.11a), resulting in the LMOs moving further apart and transport being suppressed (Fig. 4.10j). Together, this yields rectification, as can be seen in Fig. 4.12b (blue curve). This approach combining water molecules and the electric field is an important find as it yields a substantially larger asymmetry in the orbital alignment, thus leading to a RR of 40. The effectiveness of this approach is substantiated when comparing it to the simpler approach where we do not take into account the movement of the water molecules or counter-ions as function of the electrical field, which gives us a RR of 15.

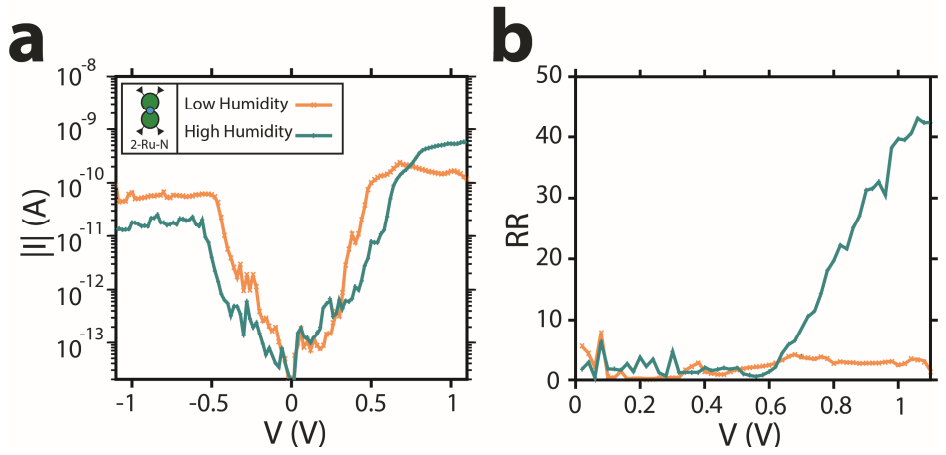

Figure 4.12: Current (a) and RR (b) calculated for the **2-Ru-N** complex with and without water. In the former case, energy splitting of the LMOs leads to asymmetric I-Vs.

Our model is similar to that of Perrin et al(*87*). However, there the asymmetry was built into the molecule chemically, whereas here we start with a symmetric two-level system, the asymmetry being induced externally, via water molecules screening the counter-ions.

For the dry case of **2-Ru-N** (i.e. with no water molecules added), the calculated |I|-V-curves are symmetric (Fig. 4.12a), which is a reasonable result as there is no physical reason for any asymmetry to occur in the system. Thus, our model is in line with experiment, indicating that our model captures the essential physics.

4.4.2.1 Effect of ion displacement

From DFT calculations, we have observed that a change in the displacement of the counter-ions at the tip side in the presence of water removes the degeneracy between the LMOs, which leads to rectification, as the model in Figure 4.10 illustrates. Although qualitatively reproducing the experimental results, our model does underestimate RR-values.

We have included only 28 water molecules for now due to hardware restrictions. To arrive at a more complete picture, the model can be extended. We can mimic the addition of more water molecules by extrapolating the counter-ion displacement (see Figure 4.13), anticipating that the addition of more water will displace the ions further (more than the displacement of 0.25 Å that we calculate with 28 water molecules). Note that the change in displacement is done without taking into consideration the effect of the electric field during bias sweeping. Thus, we calculate the I-V spectra while fixating the counter ion positions (and excluding the explicit water molecules), after which we reiterate with incrementally increasing steps of the counter ion displacement.

In Figure 4.13, we show how the main orbitals involved in transport change upon moving the counter ions away from the Ru centers along the axis connecting these centers. It can be seen that for an ion displacement of 0.5 Å, the HOMO and HOMO-1 orbitals are localized, indicative of the two LMO chemical potentials being non-degenerate, which leads to a significant rectification. As the ion displacement is further increased to 1.0 Å, it also moves the originally lower lying HOMO-2 and HOMO-3 levels relatively higher in energy, eventually surpassing the HOMO-1 (Fig. 4.13c).

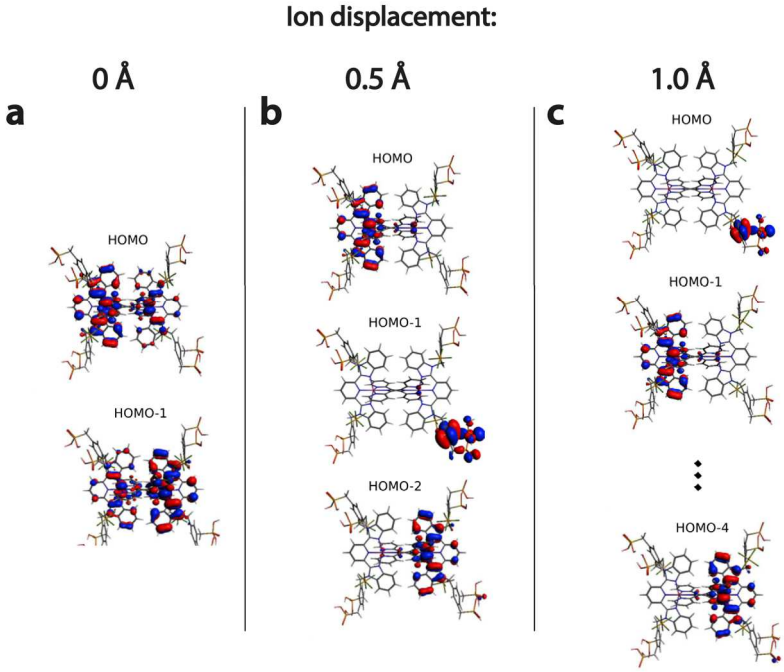

Figure 4.13: Comparison of the molecular orbitals of the **2-Ru-N** complex when the counter-ions at the right side of the system are displaced at distances of 0.0 (a), 0.5 (b) and 1.0 Å (c). These calculations were performed without considering water molecules. It is clear that when the counter-ions are displaced, the HOMO and HOMO-1 energy levels are not degenerate anymore.

Using NEGF we perform electron transport calculations for ten different ions-Ru distances between 0.0 Å and 1.0 Å. In Figure 4.14, we show the current and the rectification for the three distances used in Figure 4.13 in the absence of water.

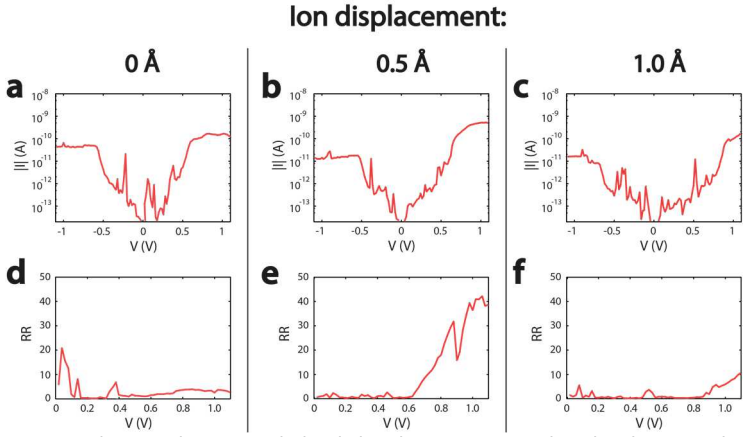

Figure 4.14: Comparison between the current calculated when the counter-ions at the right side (i.e. tip side) of the system are displaced at distances of 0.0 (a), 0.5 (b) and 1.0 Å (c) with their respective rectification ratios in (d), (e) and (f).

An analysis of the rectification ratio calculated at 1 V as a function of the ion displacement shows that the maximum rectification is close to 40 and it is achieved at 0.6 Å. For distances larger than 0.6 Å the rectification decays because the energy difference between the left LMO and right LMO requires higher voltages to achieve a sizeable current (Figure 4.14). In addition, some orbitals localized on the ions or the phosphonic acids with energies in between the two LMOs start influencing the conductance properties (Figure 4.14c).

Now, we can plot the RR (at 1 V) as a function of ion displacement, as shown in Fig. 4.15 (black line with red square data points). In the calculation done with 28 explicit water molecules as stated before, we have found the ion displacement to be 0.25 Å at 0 V (red dot in Fig. 4.15).

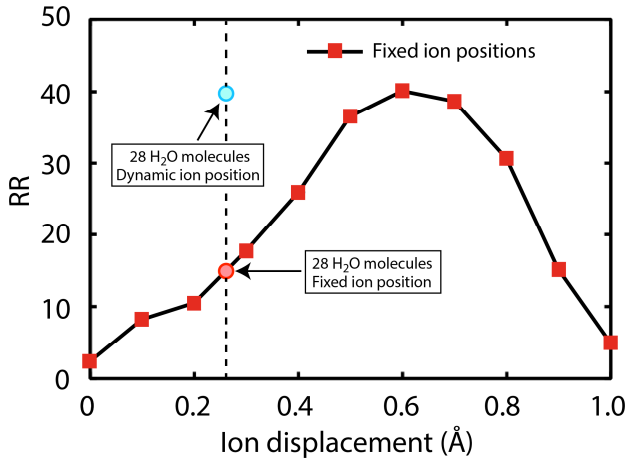

Figure 4.15: Rectification ratio as a function of the (fixed) ion displacement calculated for a bias equal to 1.0 V. It can be seen how the rectification increases and achieves a maximum at 0.6 Å. Also shown for reference is the calculated RR at 1.0 V of Fig. 4.14 (blue dot) with the dynamic approach, and without the dynamic approach (i.e. fixed ion position) (red dot).

Without taking into account the effect of the electrical field on the water molecules and counter ions during the bias sweep, this corresponds to a RR of roughly 15. However, if we account for the movement of the counter ions and water molecules with the 'dynamic' approach for the same counter ion displacement at 0 V (blue dot of Fig. 4.15), the RR is higher at around 40. Furthermore, by extrapolating the ion displacement (by adding more water molecules), we can note that there is a potential to achieve higher RR values, probably around 100, but this has not been confirmed by calculations.

Even this extrapolation underestimates the RR values by well over one order of magnitude. It may be that there are other, hopping-like effects during electron transport that were unaccounted for. After all, we have primarily used an elastic transport model until now. To check for this, we have investigated temperature-dependent effects on the conductance in both humid and dry conditions, the presence of which will provide a strong evidence for hopping-like transport and thus, a possible explanation as to why our model is failing quantitatively (although qualitatively it is consistent with our data).

4.4.2.2 Temperature dependence of the conductance of 2-Ru-N (high humidity)

We have performed I(V,T) measurements (as described in Chapter 3.5.2) in high humidity and have plotted the data in the Appendix Fig. A.7. Unfortunately, these data cannot be straightforwardly interpreted. To summarize, we know that the conductance at negative bias values of **2-Ru-N** is several orders of magnitude lower than positive bias values in high humidity. We find that at progressively higher temperatures (locally on the sample, using the Peltier element), the conductance at negative bias values increases significantly, thereby lowering the RR value at 0.9 V to ~10. This large change can be explained by either an intrinsic temperature dependent property of the **2-Ru-N** molecule, or by the lowered local humidity due to high sample temperatures. The latter would then effectively make the local environment 'dry' which gives close to symmetric I-Vs. From our analysis in Appendix Fig. A.7, we have found that the

drop in RR in higher local is indeed likely to be caused by the drop in local humidity due to increasing local temperature.

4.4.2.3 Temperature dependence of the conductance of 2-Ru-N (low humidity)

To exclude possible effects resulting from humidity, we have repeated the experiment in dry conditions. It is however, difficult to determine whether transport is dominated by either hopping or tunneling contributions. We will discuss our findings below.

We have performed temperature-dependent measurements on **2-Ru-N** junctions under dry conditions between 298 K and 343 K. Shown in Figure 4.16a is an Arrhenius plot of the conductance dependency measured at 0.3 V and 0.9 V. We can note from this figure that when measuring the conductance at a bias voltage of 0.3 V, there is a stronger dependency on the temperature compared to measuring the conductance at a bias voltage of 0.9 V. A temperature-dependence could be the result of activated transport or of coherent transport with Fermi-distribution broadening. The question is hence if we can distinguish the two. If we were to assume hopping transport, our data set for V=0.9 V yields an activation energy of E_a=0.1 ± 0.3 eV, whereas at V=0.3 V we find an activation energy of E_a=0.3 ± 0.3 eV. We can compare the latter value to what we find for a two-site model calculation based on Fermi-distribution broadening (see Appendix Fig. A.8 for details). Plotting the results for the latter model in Fig. 4.16b in the same fashion, we can note a discrepancy of the conductance values of several orders of magnitude with experimental case (Fig. 4.16a). Nonetheless, we can obtain an 'activation energy' (note: strictly speaking, we cannot use the term activation energy in a context where the current is determined by an elastic tunneling contribution) E_a of 0.04 eV for V=0.9 V and 0.12 eV for V=0.3 V, which also within the error bars of the activation energy data set. This suggests that based on the slope of the conductance-temperature curve, we cannot distinguish our experimental data set from that of a two-site model, within error bars.

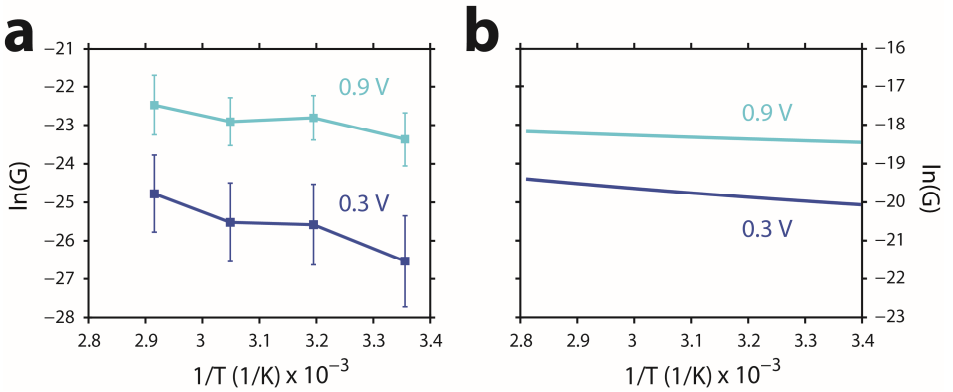

Figure 4.16: ln(G) plotted against the inverse temperature for the experimental result (a). An activation energy E_a = 0.3 ± 0.3 eV can be extracted for 0.3 V and E_a = 0.1 ± 0.3 eV for 0.9 V. In plot (b) ln(G) calculated for a two-site model with thermal broadening of the Fermi energy, is plotted as a function of the inverse of the temperature.

Furthermore, as discussed before, temperature-dependent measurements in humid conditions do not yield an intrinsic temperature dependence (see Appendix Fig. A.7). Taking also the very positive redox potentials of **2-Ru-N** (Fig. 3.2) into account, we conclude that it is difficult to assign the mechanism as either a purely hopping phenomenon or a Fermi broadening contribution to coherent transport. Most likely our system is close to the cross-over between both regimes(*80, 89, 93*). In fact, our data set may well serve as a benchmark for future theory development in this cross-over region.

4.4.3 Incorporating tip radius and force dependent data

Experimentally, we also find that the RR-values in humidity depend on tip radius and applied force. Clearly, this is not captured by our (microscopic) model. Hence, let us revisit the model of Capozzi et al.(*62*) and Cheung et al.(*86*) which show that an asymmetry in the electrodes' areas (tip and substrate) can cause an asymmetric potential distribution and an asymmetric double layer at the interfaces, even though

pressure dependence was not considered. However, in those references, a single molecule in an electrolyte is considered, whereas we have a full SAM. The latter will prevent the electrochemical double layer from reaching the ITO-substrate. This may explain why we do not see rectification for **1-Ru-N** and **1-Ru-Py**, as expected within the picture of Capozzi et al.(*62*) and Cheung et al.(*86*).

To connect the single-molecule calculations presented above to the macroscopic situation in which we perform the experiments, we present a tentative model based on the Gorsky effect. Specifically, we aim to understand why the RR-values increase as the force applied is decreased, for **2-Ru-N** SAMs in high humidity. Key is the fact that we use a (locally) spherical tip, which hence asserts a pressure on the layer that varies radially. This pressure influences, i.e. decreases, the local water concentration, see Fig. 4.17.

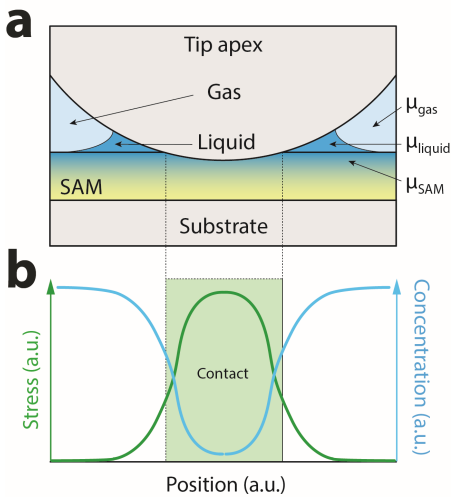

Figure 4.17: (a) Schematic impression of a junction during a C-AFM experiment, illustrating our tentative Gorsky-effect model. Directly beneath the tip apex, where the SAM is contacted, a pressure (gradient) exists, the size of which depends on both the force applied and the tip radius. Enhanced local stress leads to outward diffusion of H_2O. In steady state, this results in a water concentration gradient with a sign opposite of that of the pressure (stress) gradient (b). Hence, the molecules in the center are relatively 'dry', which results in more symmetric transport properties. This simple model thus predicts lower RR values for higher applied forces.

Let us now go into a bit more detail. Our experimental procedure for measuring in high humidity is as follows: At the start, the tip is up, not touching the SAM and we increase humidity. In that situation, water molecules start to cover the **2-Ru-N** layer from the top, until a steady state is reached. In steady state, the chemical potential of the water molecules $\mu_{H_2O,SAM}$ both on and inside the SAM equals the chemical potential of the water molecules in the vapour. The latter situation is given by:

$$\mu_{H_2O,SAM}(T) = \mu_{H_2O,\,vapor}(T) = kT \ln\left(\frac{p_{H_2O}}{p_0(T)}\right) \qquad (1)$$

Where p_{H2O} is the partial pressure of water in the chamber, $p_0(T)$ is a reference pressure, T is temperature and k is Boltzmann's constant. The latter part can be rewritten to include the relative humidity h(T):

$$\mu_{H_2O,\,vapor}(T) = kT \ln\left(\frac{p_{H_2O}}{p_{sat}}(T)\right) + kT \ln\left(\frac{p_{sat}}{p_0}(T)\right) = kT \ln\big(h(T)\big) + b(T) \qquad (2)$$

Where $p_{sat}(T)$ is the vapour (i.e. saturation) pressure of water at temperature T, while b(T) is a constant for a certain T. These two equations together demonstrate that a further increase in humidity will lead to a higher steady-state concentration of water molecules on and in the film.

Experimentally, we then contact the film by pressing down the tip. If we do this with negligible force, the water content on/in the film will not change. The (few) molecules contacted will show rectification

behavior, due to displacement of the counter-ions (see the model in our main text and above). This changes as we exert a significant force. In that case, there will be a pressure (stress) that decreases from the tip apex outwards (see Fig. 4.17). The local stress $\sigma(r)$ increases the local chemical potential proportionally, breaking down the steady state (NB: r denotes the position in the film; r=0 is defined exactly below the tip apex). As a result, the water molecules start to diffuse outward, a phenomenon called the Gorsky effect(*94*). To model this, the outward flux of water molecules $\boldsymbol{J}(\boldsymbol{r})$ is written as the sum of two opposing 'forces': (i) the gradient of the concentration of water molecules in the SAM, $c_{SAM}(r)$; and (ii) the gradient in stress(*94, 95*):

$$\boldsymbol{J}(\mathbf{r}) = -L\left(\nabla\mu_{H_2O,\,SAM}(T) + \Omega_{H_2O}\cdot\nabla\sigma\right) = -L\left(\frac{kT}{c_{SAM}}\cdot\nabla c_{SAM} + \Omega_{H_2O}\cdot\nabla\sigma\right) \qquad (3)$$

Here, Ω_{H_2O} denotes the effective volume a water molecule occupies in the film. For this situation, a new steady state is reached once the total chemical potential for water is the same everywhere (for the vapour, the possible water liquid neck, and for the water molecules inside the film). In that case, the flux vanishes everywhere, i.e. $\boldsymbol{J}(r)=0$, and we find:

$$\frac{kT}{c_{SAM}}\cdot\nabla c_{SAM} = kT\cdot\nabla\ln(c_{SAM}) = -\Omega_{H_2O}\cdot\nabla\sigma \qquad (4)$$

In other words, the concentration gradient will have a sign opposite to the stress gradient. From this we deduce that the water concentration will be minimal in regions of maximal stress, i.e. beneath the tip apex. Referring to our single-molecule model, this implies that the molecules in the center, being relatively 'dry', will show relatively symmetric individual IV-curves with low RR-values. For the ensemble, in a simplified view seen as a set of molecules in parallel, this will lead to lower RR values too, as compared to the case where a negligible force is exerted onto the SAM.

Hence, this simple picture qualitatively explains why we see an increase in RR values upon decreasing the force during an experiment. An estimation of the change in the local chemical potential beneath the tip apex due to the stress component gives a value of ~20 meV. Indeed, this comparable the thermal energy kT. We do refrain from a more quantitative model, however, as this requires very detailed information about the relatively complex system we study experimentally.

4.5 Conclusion

We have shown that the I-V-characteristics of **2-Ru-N** SAMs change reversibly between symmetric (RR near unity) and diode-like (RR> $10^{3.8\pm0.6}$) when the local relative humidity is varied. Alternatively formulated, water can act as an external stimulus, switching rectification values RR with an on-off ratio ~10^4. Although modeling is challenging due to the complex composition of the system, a coherent tunneling picture with two LMOs in series is consistent with our experimental data. Yet, quantitatively the explanation of the large RR observed in the experiment requires further refinement of our model.

These highly sensitive **2-Ru-N** SAMs form proof-of-principle nanoscale sensors, with their functionality based on the exact molecular structure chosen.